Available online at www.sciencedirect.com

ScienceDirect

Acta Materialia 78 (2014) 254–270

Acta MATERIALIA

www.elsevier.com/locate/actamat

In situ laminography study of three-dimensional individual void shape evolution at crack initiation and comparison with Gurson–Tvergaard–Needleman-type simulations

Toshiyuki Ueda [a,*], Lukas Helfen [b,c], Thilo F. Morgeneyer [a]

[a] MINES ParisTech, PSL Research University, MAT – Centre des matériaux, CNRS UMR 7633, BP 87, 91003 Evry, France
[b] ANKA/Institute for Photon Science and Synchrotron Radiation, Karlsruhe Institute of Technology (KIT), PO Box 3640, D-76021 Karlsruhe, Germany
[c] European Synchrotron Radiation Facility (ESRF), BP 220, F-38043 Grenoble Cedex, France

Received 24 December 2013; received in revised form 11 June 2014; accepted 14 June 2014

Abstract

The mechanisms of fracture and individual void evolution in ductile thin (1.0 mm) sheet metal (AA2139 T3) under mechanical loading were investigated using in situ synchrotron-radiation computed laminography (SRCL) and finite element simulations. The in situ SRCL data allowed for quantifying the evolution of individual voids at different positions on the flat and slant fracture surfaces with different associated stress and strain histories. The evolution of parameters such as void volume, their Feret dimensions and void reorientation angle was investigated. The result shows that voids on the flat crack surface do not show reorientation whereas voids on the slant crack surface orient towards the slant crack surface. However, most of their surface does not lie on the final slant crack. It is also shown that Gurson–Tvergaard–Needleman simulations overpredict the void growth compared to the measured values.

Keywords: Ductile fracture; Void growth; Synchrotron radiation; In situ laminography; Aluminium alloy

1. Introduction

Fracture toughness of ductile materials is a crucial criterion to design lighter structures for transportation applications [1]. Ductile materials usually fail as a result of microscopic void evolution processes such as void nucleation, growth and coalescence [2]. Voids nucleate at inclusions or second-phase particles during the fracture process and also pre-exist in a material in the form of hydrogen micropores due to the manufacturing process. In the case of a thin sheet metal, which is widely used in structures for transportation applications, fracture initiation at the notch or pre-crack root typically commences with the formation of a flat triangular fracture surface, whose normal corresponds to the loading direction. Once the initial flat fracture surface is formed, the crack tilts and propagates with a slant fracture surface with an angle of ~45° to the loading direction after some extension [3]. Experimental results [4] indicate that on the flat fracture surface, fracture is governed by the growth of primary voids nucleated on large constituent particles or by growth from initial porosity due to the fact that hydrostatic pressure is dominant, whilst on the slant fracture surface, void growth seems limited and void sheeting, i.e. sudden nucleation and coalescence of, i.e. sub-micrometre voids in a localised area, can be observed. Despite the research that has gone into the study of the mechanisms of transition from the flat-to-slant fracture surface, fundamental aspects of the mechanisms are still not fully understood [1,5–7].

* Corresponding author.
E-mail addresses: toshiyuki.ueda.0730@gmail.com, toshiyuki-ueda@mail.nissan.co.jp (T. Ueda).

http://dx.doi.org/10.1016/j.actamat.2014.06.029
1359-6454/

In recent studies, three-dimensional (3-D) finite element (FE) modelling has played an important role in investigating void evolution under different stress states. The flat to slant fracture transition in steel was investigated using the computational cell technique and the Gurson–Tvergaard–Needleman (GTN) model under stable tearing conditions prescribing the flat to slant crack path with a layer of Gurson-type elements [8]. The result showed that the energy dissipation rate reaches a minimum value in the case of the slant fracture for a final tilt angle equal to 45°. However, modelling void behaviour in this phenomenon is still challenging. Historically, models for void growth [9,10] were proposed with the assumption of isotropic void growth from an initial isotropic spherical void. However, the behaviour of voids in a strain localization band cannot be reproduced by these models with respect to shape change. The crack typically remains flat using these kinds of void growth based damage models [3]. By accounting for shear based void nucleation, the crack may become slanted [7]. Attempts have been made on modelling to account for anisotropic void growth. Axisymmetric void growth from an initially axisymmetric ellipsoidal void with respect to the primary loading direction was also modelled [11,12], or non-axisymmetric and anisotropic void growth from a generic initial 3-D ellipsoidal void [13]. A comparison with experimental observations is needed to validate model predictions. Destructive two-dimensional (2-D) sectioning of stopped tests or post-mortems provide insight into the damage state at given mechanical states (e.g. [14]) but the evolution of damage is hard to achieve with these methods. As a result there is limited 3-D in situ insight into the microstructure during fracture in the literature. The objective of this work is to provide experimental data for comparison with models. A comparison with simulations using a rather classical GTN-type model is made.

Aiming at investigating microscopic mechanisms of fracture, X-ray computed tomography (CT) has been used to observe in situ the 3-D damage evolution in ductile engineering materials [15–18]. However, a drawback of CT is that the shape of specimens is limited to small matchstick-like ones with cross-sections of the order of $1 \times 1\ mm^2$ due to the fact that a large variation in X-ray transmission while rotating specimens should be avoided for better reconstruction of a 3-D image from 2-D projections. Therefore, the technique is not well suited to in situ measurements of a plate-like specimen, i.e. extended in two directions and thin in the third one [19,20]. Moreover, plastic zone sizes in the specimens for CT are not compatible with many key engineering failure situations where plastic zone sizes may reach the order of several millimetres. With the recent progress in synchrotron laminography [19,20] it has become possible to observe in situ and in three dimensions damage evolution in plate-like objects [21]. Ductile crack initiation and propagation in a 2139 Al alloy have been studied for the first time in three dimensions and in situ inside a thin (1.0 mm thickness) sheet material with boundary conditions close to those of structures in service and close to standard mechanical tests to assess the tearing resistance [22]. In this study the source data obtained in the experiment [22] are used.

The aim of this work is to visualise and to quantify the microscopic behaviour of selected voids during fracture in a thin-sheet engineering material. The experiment result [22] provides detailed 3-D information concerning void evolution in the material. In the first step, the void evolution in four different zones in a specimen is visualised to show different void volume and shape changes under different stress–strain histories. Then finite element simulation using a rather classical extended Gurson model [10,23] is performed to estimate the stress and strain states in the specimen at the four locations. Making use of these results, the void evolution at the four different locations is quantified in terms of void volume fraction and void shape change and discussed with respect to stress triaxiality obtained from simulations. Finally, the contribution of the voids and their shape change to crack formation is investigated.

2. Experimental

2.1. Material

The material used in this study is an Al–Cu–Mg (AA2139) aluminium alloy in naturally aged T3 condition for aerospace applications. The chemical composition of the material is shown in Table 1 [24]. The material was provided as a sheet metal with 3.2 mm thickness and was subsequently machined down symmetrically to 1.0 mm. The mechanical properties of the material in terms of stress and strain curves and ductile tearing curves are given in Ref. [23]. In the following, the rolling direction is referred to as L, the long transverse direction as T and the short transverse (thickness) direction as S.

The size and distribution of pores and particles in the material have already been assessed from tomographic data via Feret dimensions of pores and particles and Feret dimensions of 3-D Voronoi cells around pores and particles [23] (see Table 2). These values would approximately double when only pre-existing voids are considered. Those may contribute most to the failure process [25]. The material has an initial void volume fraction of ~0.34%. This value has been obtained by tomography [23] and it has the same order of magnitude as values obtained in Refs. [4,26]. These pores have been identified as hydrogen micropores [25,27]. The mean Feret dimensions of pores is maximal in the L direction, which obviously shows the effect of the rolling process on the formation of void shape. The Voronoi cell dimensions of ~25 μm indicate isotropic void and particle distribution in the material. The grain size of 60 μm in the L direction, 52 μm in T and 24 μm in S have been obtained from optical microscopy on etched sections using a mean linear intercept method [24]. The grain size in each direction also shows the effect of the rolling process on

Table 1
Chemical composition limits of the AA2139 alloy in wt.% (after Ref. [24]).

Alloy	Si	Fe	Cu	Mn	Mg	Ag	Ti	Zn
2139	⩽0.1	⩽0.15	4.5–5.5	0.20–0.6	0.20–0.8	0.15–0.6	⩽0.15	⩽0.25

the material. Further details on the microstructure of the material were reported previously [22,28].

2.2. Mechanical in situ test

The tearing in situ test was performed on a flat-notched specimen with a width of 60 mm, a height of 70 mm and a thickness of 1.0 mm (see Fig. 1). A notch was machined by wire electrical discharge machining (EDM) resulting in a radius of 0.17 mm. The initial notch length to width ratio is 0.6. The loading was applied in the L–T configuration via opening the notch mouth with a displacement controlled two-screw opening device. Stepwise monotonic loading was applied between different laminography scans. A scan was performed before every loading step and the total number of scans was ~20. The region of interest (ROI) for the scan was initially set close to the notch and was moved along with propagation of the crack tip to image the damaged material ahead of the crack tip. An anti-buckling device was used to prevent the thin-sheet specimen from significant buckling and out-of-plane motion in the compression zone. Further details of the mechanical testing were reported previously [22,28].

2.3. Laminography

Synchrotron-radiation computed tomography (SRCT) is particularly adapted to imaging of one-dimensionally elongated, i.e. matchstick-like, specimens, which stay in the field of view of the detector system under rotation. In contrast, synchrotron-radiation computed laminography (SRCL) [29] is optimised towards the imaging of laterally extended, i.e. plate-like, specimens. For laminography, the rotation axis of a specimen is inclined at an angle of $\theta < 90°$ with respect to the beam direction (where $\theta = 90°$ corresponds to the case of CT). The specimen is typically turned around the normal vector of the sheet plane (see Fig. 2).

For a plate-like specimen this enables a relatively constant average X-ray transmission over the entire scanning range of 360°, which in turn allows for the acquisition of reliable projection data. Using a filtered back-projection algorithm [19], a 3-D image of the imaged specimen around the rotation axis is reconstructed from the 2-D projections. Although the sampling of the 3-D Fourier domain of the specimen is incomplete [19], which leads to imaging artefacts, the latter ones are often less disruptive than those produced by (limited-angle) CT [30,31].

Imaging was performed on KIT's laminography instrument installed at beamline ID19 [31] of the European Synchrotron Radiation Facility (ESRF, Grenoble, France). An inclination angle of the specimen rotation axis of ~25° with respect to the beam normal ($\theta \approx 65°$) was chosen as well as a monochromatic beam of 25 keV X-ray energy [22]. The multilayer monochromator employed for imaging has an inhomogeneous beam profile [32] and therefore is prone to introducing further artefacts (i.e. so-called "ring-artefacts") similar to the ones encountered in CT images [33,34]. Volumes were reconstructed from 1500 angularly equidistant radiographs with an exposure time of 250 ms. The size of ROI was ~1 mm^3 in volume with a voxel size of 0.7 μm. The final reconstructed volumes have a size of 2040 × 2040 × 2040 voxels. The minimum specimen to detector distance was 70 mm, leading to relatively strong edge enhancement [35] due to phase contrast. For easier data handling, all 3-D images consisting of 32-bit floating point values were converted into 8-bit grey level 3-D images using the same linear dependence. For 3-D void representation, the local minima approach based on the watershed transformation algorithm [36] and the Gaussian filter were used to segment voids. The error of 40% on void volume was estimated with the method similar to that used for void segmentation [4]. Scripts based on Python and a VTK software rendering routine were used to register the 3-D datasets and produce the 3-D images.

Table 2
Porosity and intermetallic particle content, dimensions and distribution of the AA2139 alloy (after Ref. [23]).

	Porosity	Intermetallic particles
f_v in (%)	0.34 With a variation of ±10% when setting extreme grey values	0.45 ±15% (Standard error based on repeat measurements at different locations and magnifications)

Mean Feret dimensions of pores in μm			Mean Feret dimensions of Voronoi cells around 2nd phase particles and pores in μm		
L	T	S	L	T	S
7.6	5.4	4.5	23	24	25

3. Results

In this study, void evolution will be characterised in four typical regions in the observed volume to represent behaviours of isolated void evolution during fracture (see Fig. 3). Two regions located ahead of the notch (300 μm), where the crack is both flat and slant, and two far from the notch (1100 μm), where the crack is mainly slant, were investigated. Each of these regions is additionally separated into two in terms of the thickness (S) direction due to different behaviours of void evolution along the S direction. In each region one void is extracted to show a representative behaviour of the void evolution until the crack surface is formed. The chosen voids are labelled by "close" or "far" to indicate distance from the notch, and "centre" or "surface" to indicate the position in the S direction. All chosen voids contribute to the final crack formation. Detailed information of these voids is given in Table 3. The void sizes of the four voids are not similar but they still show similar void evolution behaviour.

3.1. Crack mouth opening displacement (CMOD)

All the mechanical parameters are characterised as a function of CMOD obtained from the movement of the loading device in this study. Optical measurements (digital image correlation) on the surface such as in Ref. [37] have unfortunately not been made in this study. Definitions of CMOD, crack length (a) and local notch opening displacement ($\delta_{1.0}$ and $\delta_{0.7}$) are shown in Fig. 4a and b. Here, we chose two pairs of reference points for local notch opening displacement due to the fact that the pair with Ref-1 and 2 for $\delta_{1.0}$ cannot be captured for all loading steps as the laminography ROI was moved with the advance of the crack tip during the experiment. To estimate the accuracy of the CMOD values measured in the experiment, these three parameters are compared between the experiment and simulations (see Figs. 1, 4c and d; also see Section 3.5). In Fig. 4c the simulation and experiment results show good correspondence in terms of average behaviour of crack propagation around the notch, although simulated crack initiation occurs earlier than in the experiment. However, it can be seen in Fig. 4d that both simulated $\delta_{1.0}$ and $\delta_{0.7}$ overestimate those of the experiment. This is due to the fact that in the experiment there are effects of stiffness of the loading device, of friction between the loading device and the specimen and of crack mouth rotation during opening, which are not taken into account in the simulation. Additionally, care must be taken with $\delta_{0.7}$ due to the fact that $\delta_{0.7}$ in this study is sensitive to plastic zone shape as the pair of $\delta_{0.7}$ is located in a plastic zone. Nevertheless the discrepancies on both $\delta_{1.0}$ and $\delta_{0.7}$ between the simulation and the experiment are less than 10%, which would be small enough to use CMOD from the experiment to characterise the steps of void evolution. Furthermore, the comparison of crack propagation at the micrometre scale between simulations with experiments in terms of in situ crack propagation in a thin sheet metal is rarely made in the literature.

3.2. Isolated voids and clusters

Both isolated single voids and clusters of voids and iron-containing intermetallic particles are observed in the as-received material. The typical shapes of an isolated single void and a cluster are shown in Fig. 5a and b. The figure indicates that both the isolated single void and the cluster are clearly elongated in the L direction as discussed above and the cluster is composed of several single voids and intermetallic particles. Aggregation of single voids generally makes the volume of a cluster larger than that of an isolated single void. Hence, clusters may even play a more important role in crack formation than isolated single voids. However, void evolution in clusters in the experiment shows more complicated mechanisms in terms of void growth and coalescence. For the sake of simplicity and modelling purpose, we focus here on the evolution of isolated single voids.

3.3. Macroscopic crack propagation and void evolution

The 3-D volume images in a 140 μm thick slice stack at different distances from the notch in Fig. 6 are obtained to observe the macroscopic crack propagation behaviour. The as-received material shown in Fig. 6b has an isotropic void distribution in the T–S plane. For comparison a LOM image of a polished and etched 2-D section is given in Fig. 6a, clearly indicating the pre-existing voids. It should be noted that the intrinsic void content of the parent material is "exaggerated" by the 3-D nature of Fig. 6b, representing the void content of a thick slice of material. Crack initiation and propagation at 300 μm ahead of the initial notch position, where the crack is flat, and at 1100 μm, where the crack is slant (views α and β in Fig. 3b) are shown in Fig. 6c–e and f–h, respectively. The view orientation is in the crack propagation direction. The necking of the material close to the notch can be seen in Fig. 6c–e, whereas Fig. 6f–h shows less necking during crack propagation. Crack initiation at the middle of the specimen as a result of void growth and coalescence, and the formation of a relatively flat fracture surface, can be seen in Fig. 6d. In addition, voids close to the surfaces show reorientation, which may be caused by strain localization (see Fig. 6c and d), forming the slant fracture surface with respect to the primary loading direction (see Fig. 6e). These images show the classical flat crack tunnelling with crack propagation [1]. In contrast, it is observed in Fig. 6g that crack initiation at the middle of the specimen is no longer flat and seems to be controlled not by void growth and coalescence mechanisms but mainly by a strain concentration mechanism. Void reorientation also can be seen at voids close to the surfaces as well as those close to the middle of the specimen (see Fig. 6f and g). The slant

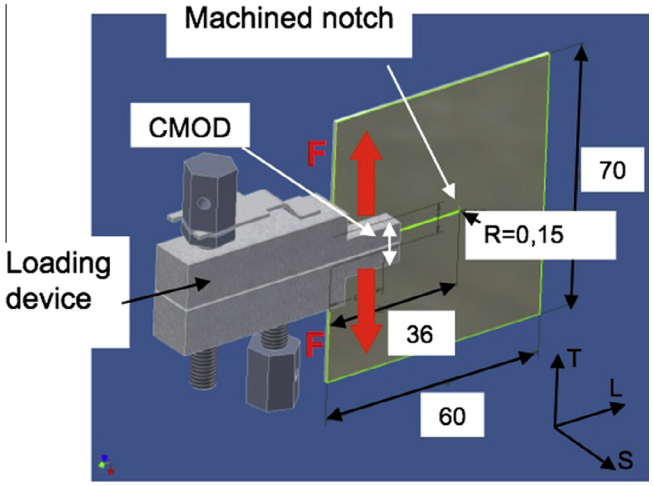

Fig. 1. Sketch of the in situ loading setup with two-screw loading device and specimen with dimensions $60 \times 70 \times 1$ mm^3. The notch length was 36 mm and its radius 0.17 mm. The CMOD was measured via movement of the two-screw loading device. The anti-buckling frame is not shown [28].

(roof-top shape here) fracture surface which is not oriented normal to the primary loading direction can be clearly observed in Fig. 6h. The apparent big void in the centre of the crack is due to local crack opening, which is at a maximum in the centre due to slight crack tunnelling. In addition, two strain localization bands are crossing here that may well increase the local level of triaxiality.

3.4. Visualisation of the evolution of single voids and their representativity

The void evolution for different load levels in terms of 2-D sections and 3-D images in the T–S and L–T planes are shown in Figs. 7 and 8 respectively. In the case of the void (close-centre), which locates close to the notch and at the middle of the specimen in the S direction, it can be seen that the void is growing larger, keeping a spherical shape, and then the shape changes into a diamond-like one, indicating that high stress triaxiality may have a dominant effect on void evolution in this region [38]. However, the void growth is not spherical before coalescence, indicating the onset of internal necking between voids. The void (close-surface), which locates close to the notch and close to the surface, shows that at the beginning of loading the void shape slightly elongates in the loading direction and subsequently reorients diagonally with an angle of ~30–40° against the loading direction. This is a result of two phenomena. One is the effect of necking due to the tensile loading condition, which facilitates elongation of the void in the loading direction before starting subsequent

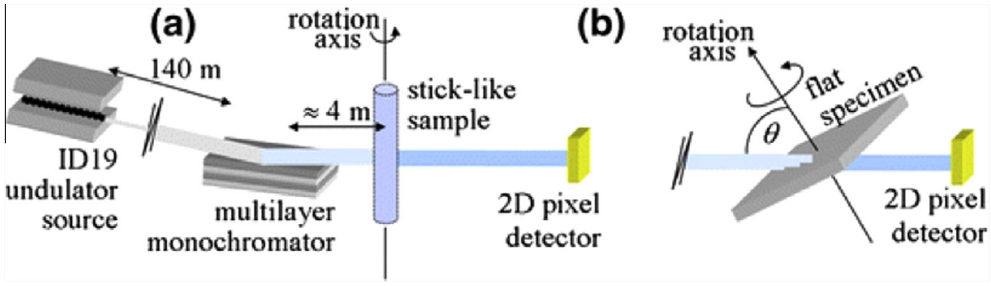

Fig. 2. Schematic views of a typical CT setup: (a) in comparison to the CL setup (b) at synchrotron beamlines with parallel-beam geometry (after Ref. [28]).

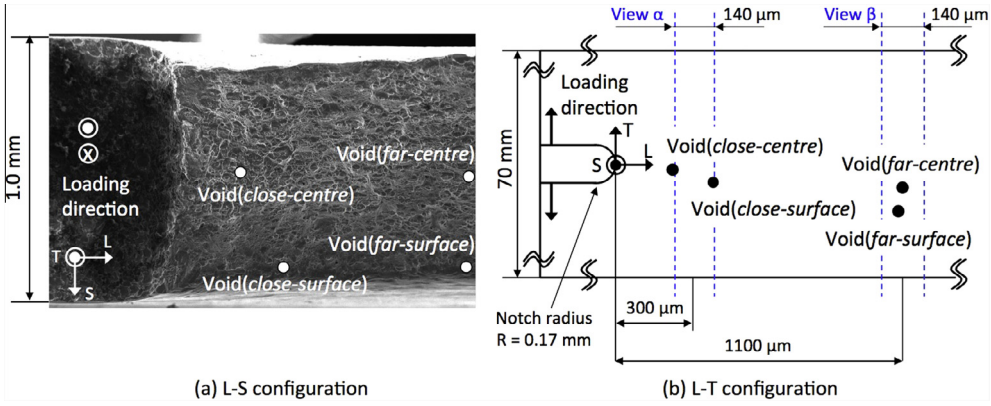

Fig. 3. Schematic representation of the specimen in the (a) L–S and (b) L–T configurations. The fractography image on (a) is obtained not by Ref. [22] but by the test with the same material, shape and test condition as Ref. [22]. The 3-D volume images with a 140 µm thick slice obtained at 300 µm (view α) and 1100 µm (view β) ahead of the initial notch position are shown in blue dotted lines. The locations of the extracted four voids to represent different void evolutions are briefly shown. (For interpretation of the references to colour in this figure legend, the reader is referred to the web version of this article.)

Table 3
Locations, dimensions and initial void volumes of the extracted voids in the four regions.

	Distance from the initial notch position in μm			Feret dimensions of the void in μm			Initial void volume in μm^3
	L	T	S	L	T	S	
Void (close-centre)	205	−3	12	16.1	9.1	8.4	492
Void (close-surface)	368	−120	478	8.4	7.7	6.3	128
Void (far-centre)	1138	−161	29	18.2	7.0	7.7	466
Void (far-surface)	1107	−396	477	4.2	4.2	5.6	34

reorientation. Another is the effect of subsequent strain localization after necking, which causes void reorientation in a strain localization band. Different behaviours of void evolution can be seen at voids far from the notch. The void (far-centre), which locates at the middle of the specimen, initially grows mainly in the loading direction. However, it starts turning toward ~30° along the way of void evolution and contributes to forming the slant fracture surface to the end. It can be observed that the behaviours of void evolution are different between the void (close-centre) and the void (far-centre) due to dependence of void evolution on stress and strain states, even though voids locate at the middle of the specimen in both cases. The void (far-centre) seems to locate in the vicinity of a position where the transition from flat to slant fracture occurs. However, there is still void growth observed which is consistent with the elevated level of stress triaxiality in the middle of the specimen. Finally, the void (far-surface), which locates close to the surface, shows that elongation of the void in the loading direction is quite limited and void shape change is controlled mainly by reorientation with an angle of ~40° due to the strain localization band around the void. In this region, the level of stress triaxiality is low. Therefore, only a little amount of void growth can be seen in this region compared to the case of the void (close-centre). However, due to the small initial void size the observation becomes harder. It is clearly seen in Fig. 8 that elongation is not significant in the L but dominant in the T direction. In one of the following sections, the behaviour of void evolution will be quantified and be interpreted with mechanical parameters obtained by image analysis and FE simulation.

For comparison, a fractography scanning electron micrograph is shown in Fig. 9. For this observation, a second sample was fractured in conditions identical to the one observed by laminography. The flat fracture surface is seen covered by large dimples, whereas the slant area is mostly covered by small dimples that may have nucleated at a second population of particles such as dispersoids at high levels of strain [4.27].

3.5. Numerical simulation

3.5.1. Damage model

The aim of performing FE simulation in this study is to simulate stress and strain field in the specimen during the experiment and then to evaluate the local evolution of stress and strain and derived parameters such as stress triaxiality at the locations where voids are observed. These are used to interpret the microscopic observation from the experiment such as void shape change and void volume fraction.

The numerical simulation has been carried out using the FE software Zebulon, which has been developed at Mines Paristech [39]. The modelling in this study is the same as the one used in Ref. [23] for the same material. The GTN model [10,40] has been used to introduce a coupling effect between plastic deformation and damage on material. Although the GTN model is able to capture the void growth stage, it can be assumed here that the GTN model is applicable to simulate the experiment that had been observed by SRCL due to the fact that the stress state of the experiment was in the positive stress triaxiality regime and above the level of uniaxial tension. In the framework of the GTN model, effective scalar stresses are defined by the following equation:

$$\Phi(\sigma_f, \sigma_{eq}, \sigma_{kk}, f_*) = \frac{\sigma_{eq}^2}{\sigma_f^2} + 2q_1 f_* \cosh\left(\frac{q_2}{2}\frac{\sigma_{kk}}{\sigma_f}\right) - 1 - q_1^2 f_*^2 = 0$$

where σ_f is the flow stress of the matrix, σ_{eq} is the von Mises stress and σ_{kk} is the trace of the stress tensor. The two fitting parameters (q_1 and q_2) [37] which influence void growth have been identified via axisymmetric, anisotropic void shape cell calculations using an elastic–plastic material law identified on the L direction tensile test [23]. f_* is the void volume fraction and represents an increased softening effect by voids during coalescence through internal necking [40]:

$$f_* = \begin{cases} f_g + f_n & \text{for} \quad f_g < f_c \\ f_c + f_n + \delta(f_g - f_c) & \text{for} \quad f_g > f_c \end{cases}$$

where f_c represents the critical growth void volume fraction for which coalescence via impingement starts and δ is an accelerating factor which represents the increased softening effect of voids once void coalescence has started.

The following equation is used to express the behaviour of void growth and nucleation:

$$\dot{f}_* = (1 - f_*)\mathrm{trace}(\underline{\dot{\varepsilon}}_p) + (A_n^1 + A_n^2)\dot{p}$$

where the first term on the right-hand side corresponds to void growth (i.e. mass conservation) and the second term corresponds to void nucleation. Here, $\dot{f}_*$ is the void

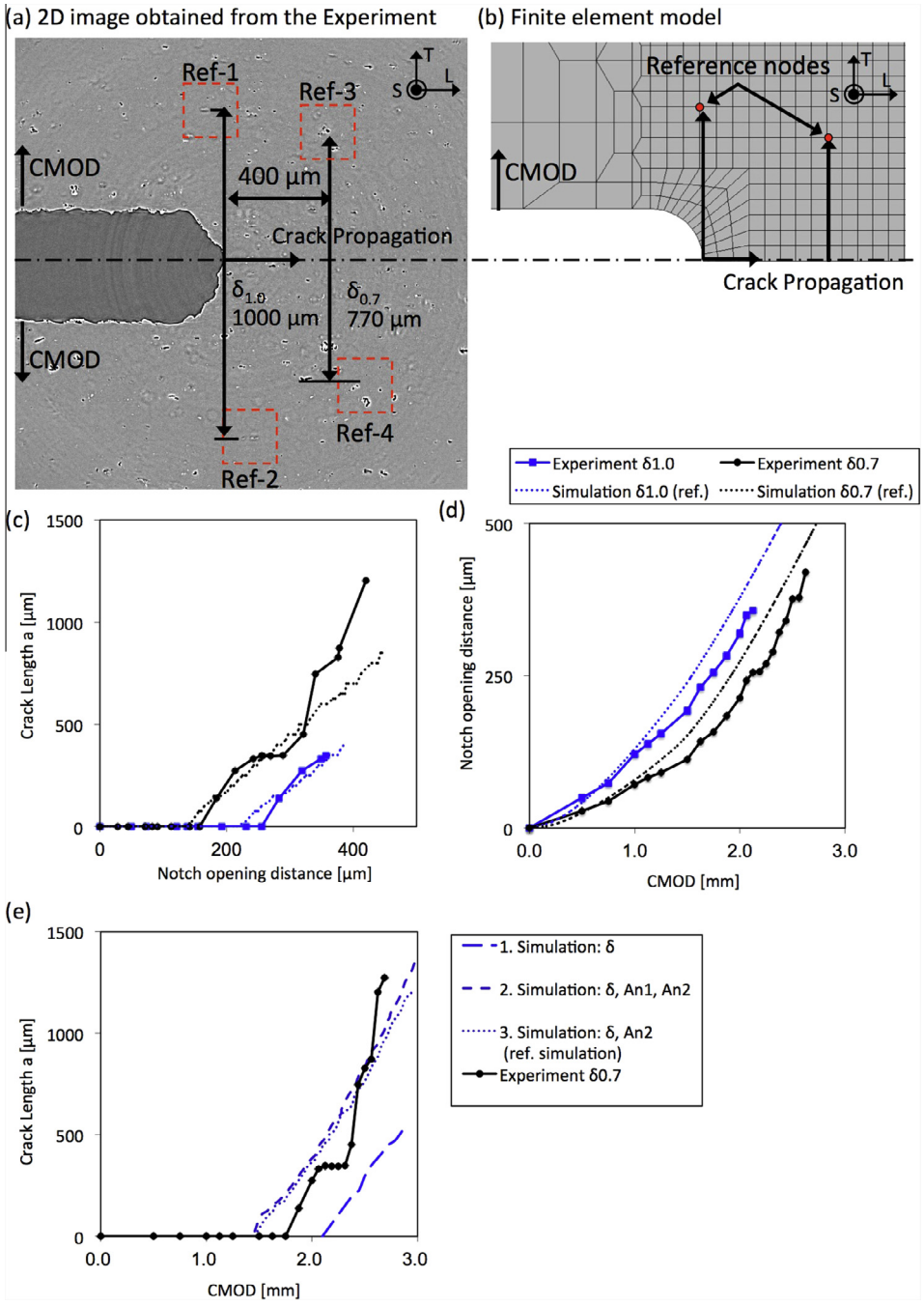

Fig. 4. (a, b) Definition of measurement on CMOD, notch opening displacement (δ1.0 and δ0.7) and crack length. (c, d) Comparison of three parameters between the experiment and the reference simulation shown in (e). (e) Simulated crack progression as a function of the CMOD for three different simulations and the experimental results.

nucleation rate and $\dot{p}$ is the strain rate. A_n^1 is a material parameter that controls nucleation rate at coarse intermetallic particles, supposing nucleation of voids around these particles up to 10% strain. A_n^2 is also a material parameter which controls nucleation at a second population of smaller second-phase particles for elevated levels of cumulated plastic strain observed in slanted areas, which appears to control fracture in low stress triaxiality. p_c^2 is a critical strain which controls the nucleation at a second population of second-phase particles. These parameters for the GTN model used in this study have already been calculated in Ref. [23] and shown in Table 4. The value of parameter A_n^2 has been changed to fit the crack progression vs. local opening graph obtained by measurements on the laminography data. This was necessary as the mesh size has been changed here to 50 µm element height with respect to the calculation carried out in Ref. [23] with 100 µm element height. In this framework the crack will progress in a flat

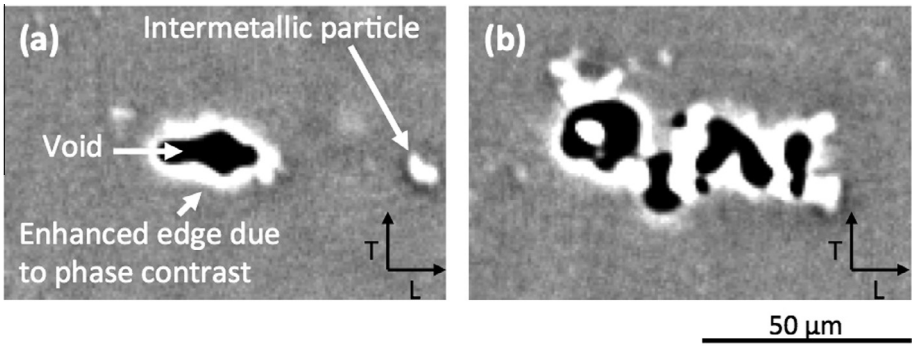

Fig. 5. 2-D sections of the as-received material in the L–T plane for (a) an isolated single void and (b) a cluster of voids and iron containing intermetallic particles. The aluminium matrix is shown in grey and the porosities can be seen in black, with white phase contrast fringes around them. The intermetallic particles are seen in white as well.

manner in the simulation. This shows that the Gurson model alone cannot capture the physics at play during slant fracture [7,41].

Fig. 4e shows the simulated crack progression as a function of the CMOD for three different simulations and the experimental results. Simulation 1, (δ) only used the Tvergaard and Needleman [40] expression for acceleration void growth after the onset of coalescence via internal necking, Simulation 2 (δ, A_n^1, A_n^2) uses δ and the two void nucleation terms and Simulation 3 (δ, A_n^2) uses the coalescence term and only nucleation of voids on the second population of particles. It can be concluded that a fairly pure form of the Gurson model only using q_1, q_2 and δ is not enough to fit the CMOD crack progression curves. The crack initiation and the progression speeds are underpredicted. It can also be concluded that the nucleation of voids on coarse particles, such as has been accounted for in the simulation via A_n^1, does hardly affect the crack progression speed as compared to the simulation using only (δ, A_n^2). For comparison with the experimentally measured void growth the simulation using (δ, A_n^2) will be utilised as this permits us to compare with a fairly "pure" form of the Gurson model up to f_c.

Here the moderate/weak anisotropy of the material is accounted for by a macroscopic plastic model for anisotropy as in Ref. [23]. However, the crack remains flat. Even for materials with stronger texture the crack remains flat when using a macroscopic plastic anisotropy model that accounts for the stronger plastic anisotropy in a GTN framework [42]. In Ref. [43] it has been found that anisotropic plasticity may help to reproduce slant localization phenomena under plain strain conditions but they could not be reproduced here. Similar localization bands as found in Ref. [41] might also be at play here and determine the slant fracture path. The origin of these bands is to be identified.

3.5.2. Distribution of plastic strain and crack propagation

A quarter of the specimen is meshed in three dimensions, as shown in Fig. 10a. The $(50\ \mu m)^3$ element size is in the fine region around the notch and gradually changes to 2.0 mm toward the upper edge of the specimen. The number of elements in the S direction is 10. The symmetry boundary condition is applied to the L–S and L–T planes. Distribution of plastic strain at the maximum load is shown in Fig. 10b. It can be seen that the typical plastic zone shape evolves in the specimen, and the specimen just close to the notch is subjected to necking, which is consistent with the observed result in Fig. 6. Simulated crack propagation is shown in Fig. 10c. It can be clearly seen that the crack propagates with a triangular shape and the fracture surface does not change to a slant one but keeps flat, as mentioned above.

3.5.3. Stress triaxiality

Simulated local evolutions of stress triaxiality at the locations where the representative voids are investigated in the experiment as a function of simulated plastic strain are shown in Fig. 11. The elements chosen here lie on the fracture path. In the case of uniaxial tension, stress triaxiality corresponds to 0.33 and pure shear to 0.0. Stress triaxiality close to the notch shows that the initial value of stress triaxiality at the centre of the specimen is ~0.9 and then increased to nearly 1.2 as plastic strain increases. In contrast, the values close to the surface decrease after the onset of plastic deformation. This is due to the effect of the necking. Necking commences close to the notch immediately after loading is applied, which facilitates an increase of stress triaxiality by plastic constraint at the centre of the specimen and reduces stress triaxiality close to the surface by plastic deformation. The initial value of stress triaxiality far from the notch is ~0.6 both at the centre and at the surface of the specimen. As plastic deformation increases, stress triaxiality at the centre of the specimen gradually increases and that close to the surface decreases. This is also due to the effect of necking, as can be seen close to the notch. The level of stress triaxiality in this simulation result is equivalent to the value reported in Ref. [3] for a Kahn specimen. It also can be observed in Fig. 11 that development of necking far from the notch is less significant than the one ahead of the notch. Therefore, stress triaxiality in this region gradually

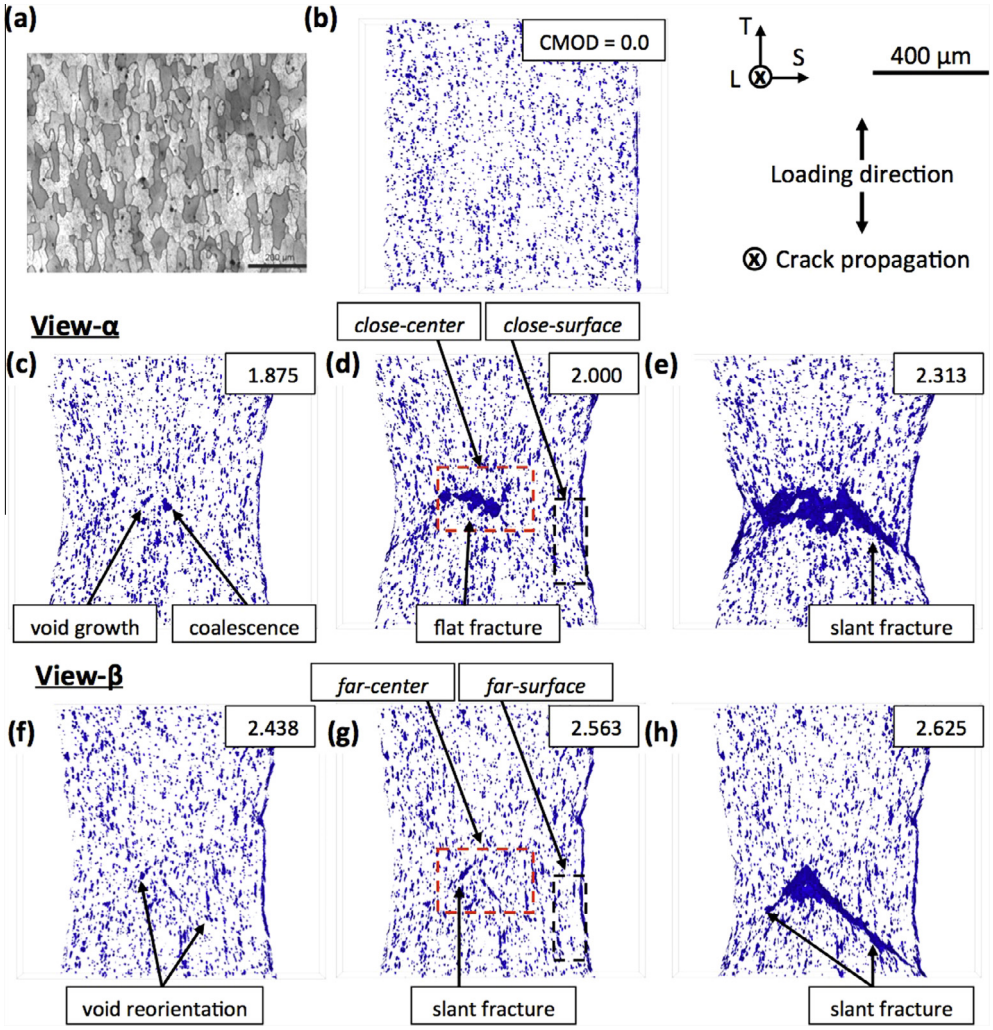

Fig. 6. (a) LOM image of a polished and etched 2-D section. 3-D volumes (140 μm thick slice) showing rendered voids in the T–S plane. (b) As-received material (view α in Fig. 3), (c) void distribution before crack initiation, (d) crack initiation and (e) crack propagation at 300 μm ahead of the initial notch position (view α). (f) Void distribution before crack initiation, (g) crack initiation and (h) crack propagation at 1100 μm ahead of the initial notch position (view β in Fig. 3). Fracture process including the supplemental loading steps is given in Videos 1 and 2.

changes compared to that close to the notch. The stress triaxiality far from the notch in the centre of the specimen increases when the crack approaches and acts as a stress concentrator.

3.6. Quantification of isolated voids evolution

The measured evolution of normalised void volume fraction (V/V_0) for the selected four voids as a function of CMOD is shown in Fig. 12a. The voids at the centre of the specimen, void (close-centre) and void (far-centre), have larger increase in void volume before fracture than the voids at the surface, void (close-surface) and void (far-surface). This is consistent with an effect of stress triaxiality which is higher at the centre than at the surface, as can be seen in Fig. 11. However, lower stress triaxiality at the surface does not prevent void volume from increasing. As can be seen in Fig. 12a, the voids at the surface also have some increase in void volume, indicating that an increase of void volume has some contribution to crack formation, even in a region close to the surface. However, the void volume increase occurs at a very late stage of loading.

The simulated normalised void evolution ($[f_0 + f_g]/f_0$) as a function of CMOD is given in Fig. 12b. It is shown up to f_c so that a comparison with an almost unmodified Gurson model is made. The ranking of void growth to fracture is consistent with the ranking of the associated levels of stress triaxiality. The void growth for void (close-centre) is substantial as it has increased 14 times. The void growth for the other voids is more limited. This is due to the fact that the levels of triaxiality for these voids are initially lower but strain is high. As a result the simulated fracture is controlled here by nucleation of voids on a second population of particles from a critical strain onwards (A_n^2). This is particularly true for the elements close to the specimen surface.

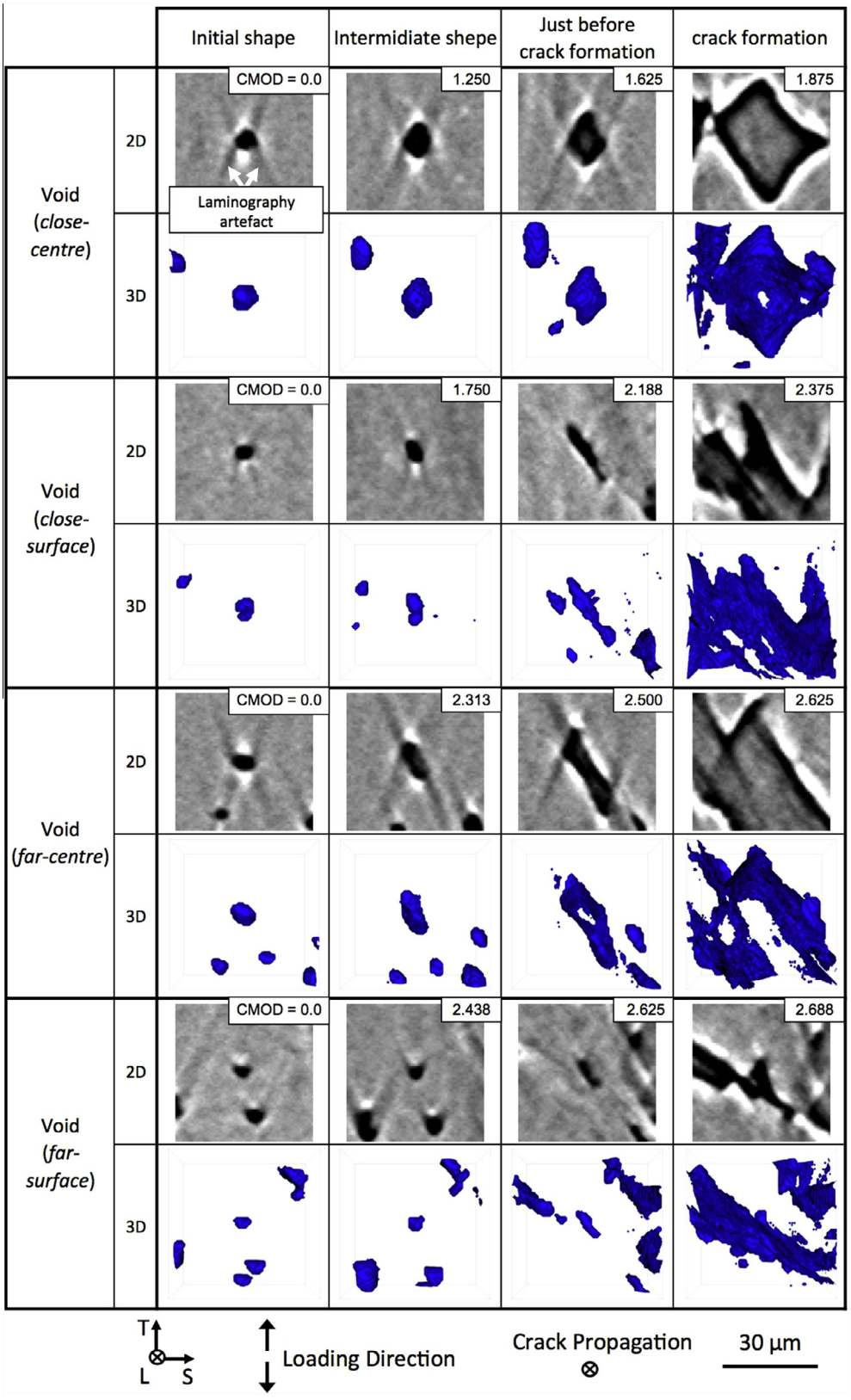

Fig. 7. 2-D sections and 3-D images with 28 µm thick of the extracted voids in the four regions for different loading steps in the T–S plane. Slicing locations of 2-D sections are at the middle of 3-D images. Void surfaces or specimen surfaces are shown in blue in the 3-D images. The centres of 3-D images correspond to those of the extracted voids. Laminography artefacts also can be seen in the 2-D sections.

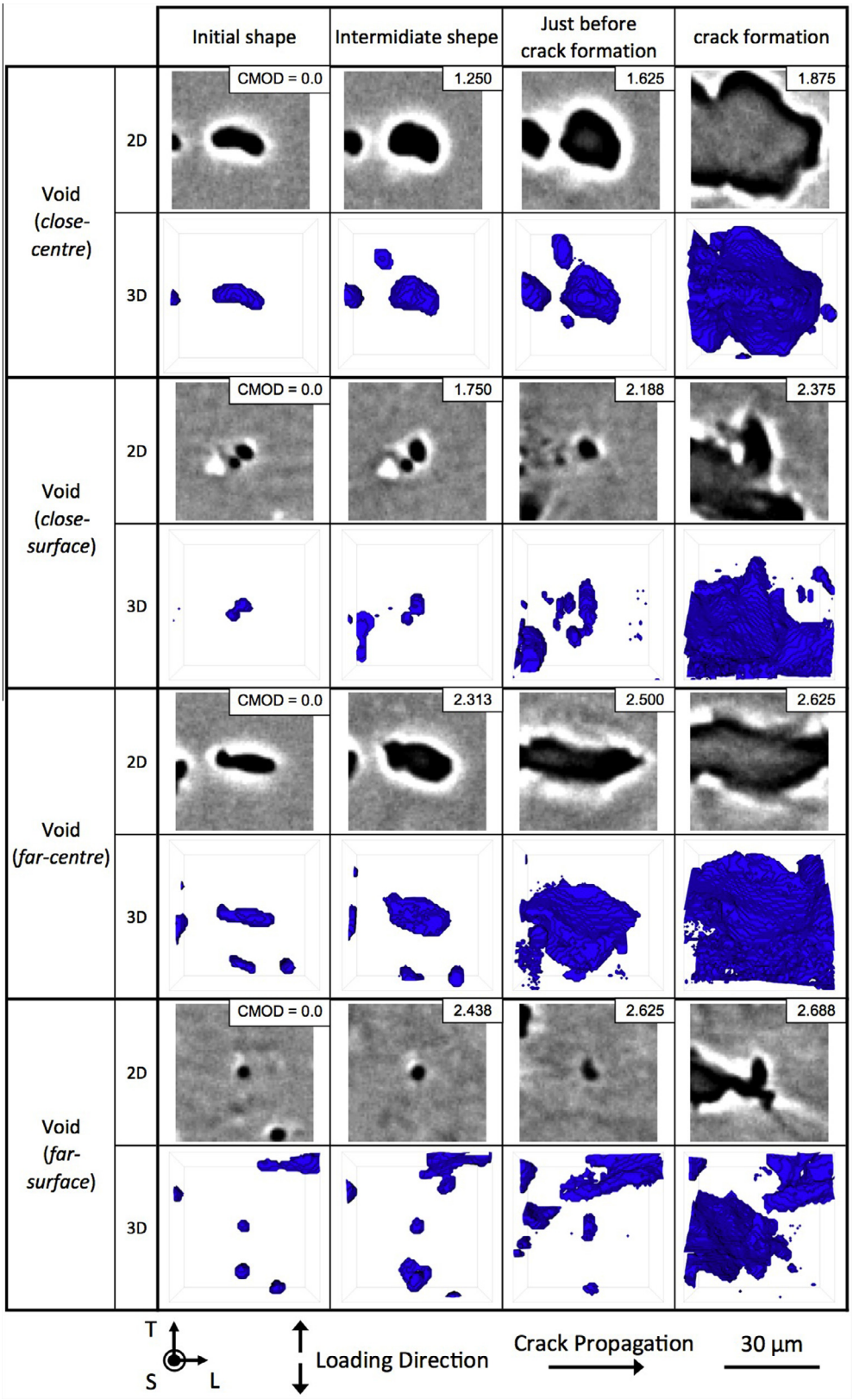

Fig. 8. 2-D sections and 3-D images with 28 μm thick of the extracted voids in the four regions for different loading steps in the L–T plane, which is the sheet plane. Slicing locations of 2-D sections are at the middle of 3-D images. Void surfaces or specimen surfaces are shown in blue in the 3-D images. The centres of 3-D images correspond to those of the extracted voids.

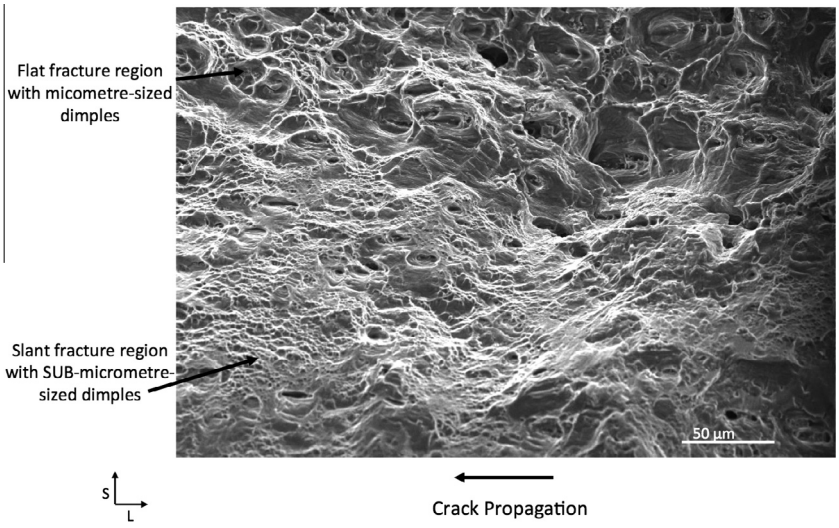

Fig. 9. Fracture surface of the flat-notched specimen, showing the flat fracture surface covered by large dimples and the slant area mostly covered by small dimples.

When comparing the measured results with the simulated ones, the most striking difference is the magnitude of growth, which is predicted 14 times for void (close-centre) and measured only 3.5 times. This strong difference might be linked to the fact that the coalescence mechanism is not correctly captured in the simulation. This may also be linked to the fact that the strain field might be poorly predicted with respect to localization phenomena [41]. The coalescence through void sheeting is only represented indirectly in the simulation. This coalescence may stop the void growth process in reality, even for the voids at high levels of triaxiality. Consistently, a void critical volume fraction at coalescence of 0.01 had already been found in Ref. [37] that is far lower than values by typical unit cell calculations.

In addition, the averaged nature of simulations and the heterogeneous nature of the real material with respect to void and particle shape/size and spatial distribution may play a role for the limited void growth in the real material.

The measured growth of Feret dimensions in material directions (L, T and S) for the selected four voids as a function of CMOD is shown in Fig. 13a–d. For all the four voids the growth in the T direction is the highest as it is the primary loading direction. The growths in the L and S direction are less significant in the case of the void (close-centre) and the void (far-centre). However, in the case of the void (close-surface) and the void (far-surface) the growth in the S direction is high due to the fact that void reorientation can be seen on voids close to the surface. It can be also seen in Figs. 12a and 13a–d that the void growth takes place at very late stages of failure. The deformation process concentrated in a slant band seems to govern failure rather than the damage/void growth and shape change process.

Table 4
Parameters for the naturally aged (T3) A2139 material simulation (after Ref. [23]).

Damage							
q_1	q_2	f_0	f_c	A_n^1	A_n^2	p_c^1	δ
1.82	0.92	0.33%	4.5%	0.045	30	0.71	3.0
Elastic–plastic behaviour							
E (GPa)	v	R_0 (MPa)	K_1	k_1			
70	0.3	237	1.43	6.90			
Plastic anisotropy							
c^{LL}	c^{TT}	c^{SS}	$c^{i=LT,TS,SL}$	b			
1.1	1.14	0.904	1.0	8			
Kinematic hardening							
C (MPa)	D						
14,947	261						

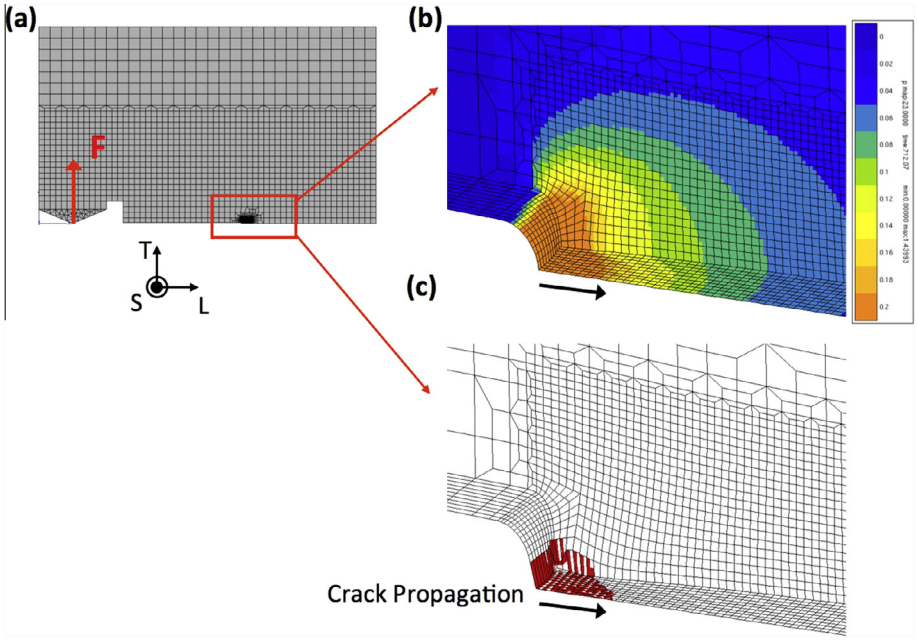

Fig. 10. (a) Entire FE mesh of a quarter of the laminography specimen with the minimum element length of 50 μm around the notch and the maximum of 2.0 mm at the upper edge of the specimen. (b) Distribution of cumulated plastic strain at the maximum load. (c) Simulated flat crack propagation (broken elements in red). (For interpretation of the references to colour in this figure legend, the reader is referred to the web version of this article.)

The evolution of void reorientation angle in the TS plane is shown in Fig. 14. It has been determined manually on the images, as 3-D image analysis techniques provided unreliable results in terms of identification of the ellipsoid major axis. The result of the void (close-centre) shows constant reorientation angle due to its strong void growth in the loading direction during loading. The other voids show void reorientation. The reorientation of the void (close-surface) and the void (far-centre) commences at less plastic strain than that of the void (far-surface). It was observed in Fig. 7 that there is elongation in the loading direction at the beginning of loading in the case of the void (close-surface) and the void (far-centre). The initial elongation may also have some reorientation. In contrast, the void (far-surface) shows quick reorientation just before crack formation, as can be seen in Fig. 7, and this phenomenon also can be confirmed in Fig. 13.

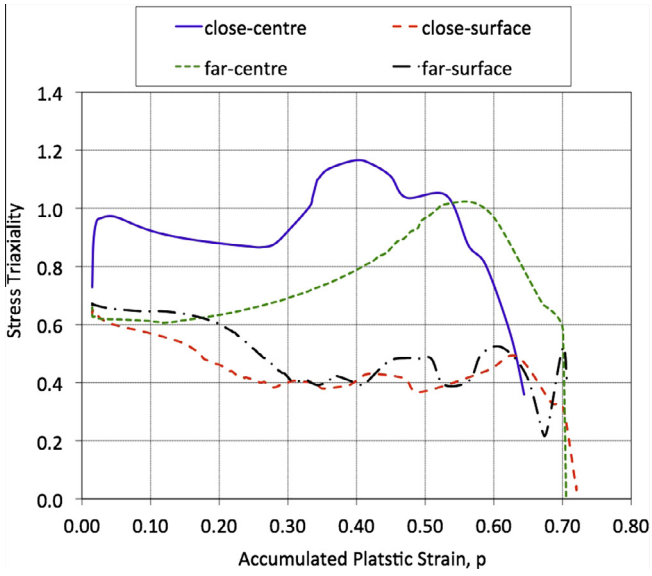

Fig. 11. Simulated local evolutions of stress triaxiality as a function of accumulated plastic strain at the locations where the voids are observed.

4. Discussion: contribution of the voids to the crack and the role of void shape and plasticity

The behaviour of void evolution regarding void volume fraction, growth of Feret dimension and void reorientation angle has been quantified. Each of the selected four voids shows different behaviour of void evolution, which is obviously caused by different evolution of stress and strain in the specimen, particularly by strain localization. The void in the flat fracture zone does not reorient but shows non-isotropic growth from non-isotropic initial shape. The three voids that lie on the slant fracture surface show reorientation towards the final crack plane. The voids on the slant surface seem to evolve under shear strain such as investigated in Ref. [44,45] via unit cell calculations. Strain concentration bands measured via digital volume correlation in conjunction with laminography [28] have been shown in a similar material for the same loading conditions in the slant fracture region [41]. In the case of tearing test, slant fracture typically develops with an angle of 45° against the loading direction. The strain localization with

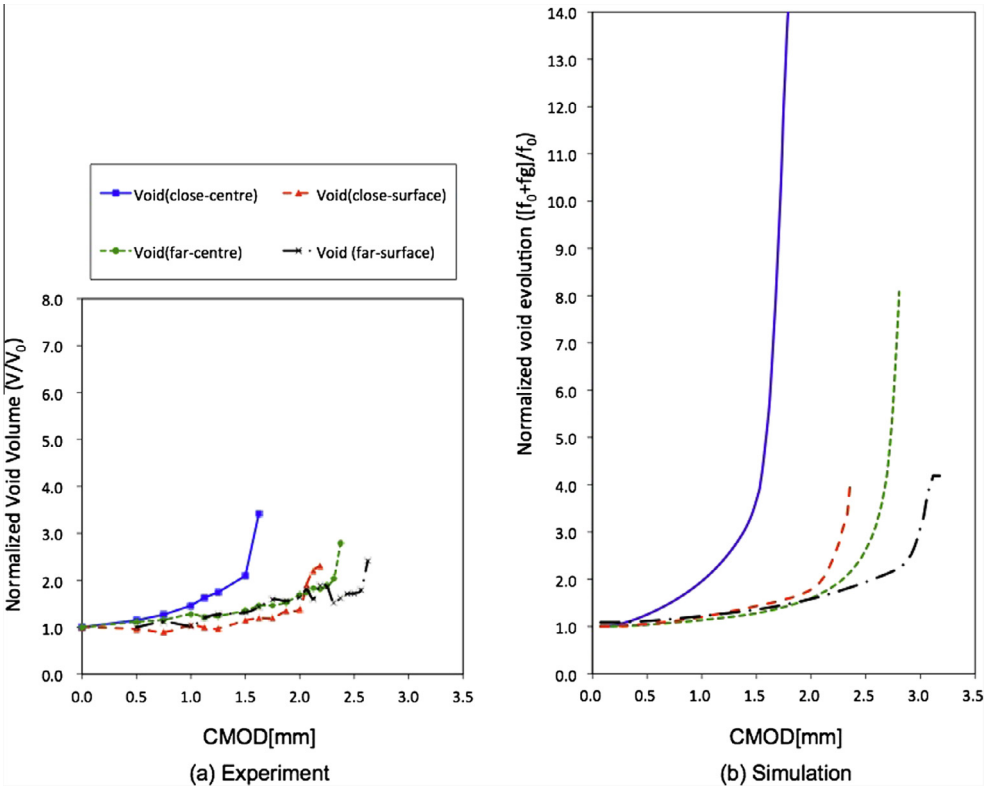

Fig. 12. (a) Measured normalised void volume and (b) simulated normalised void evolution ($[f_0 + f_g]/f_0$).

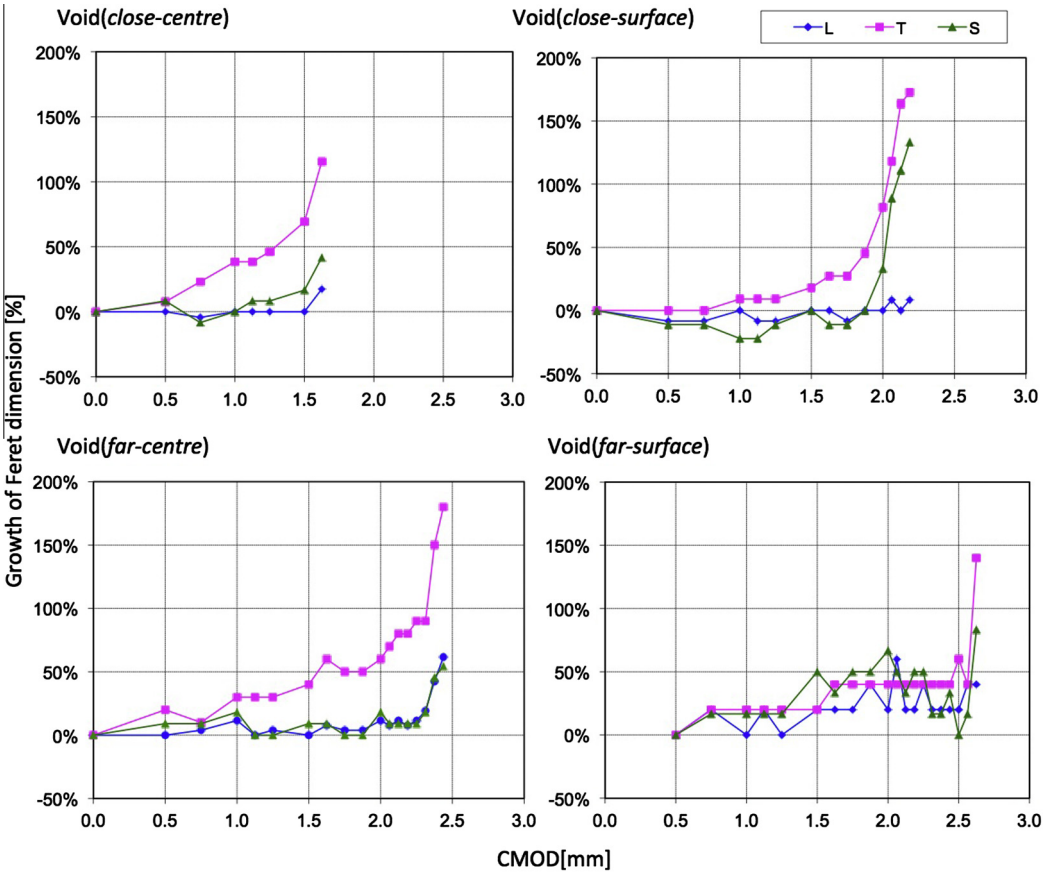

Fig. 13. Measured growth of Feret dimension for the selected four voids as a function of CMOD.

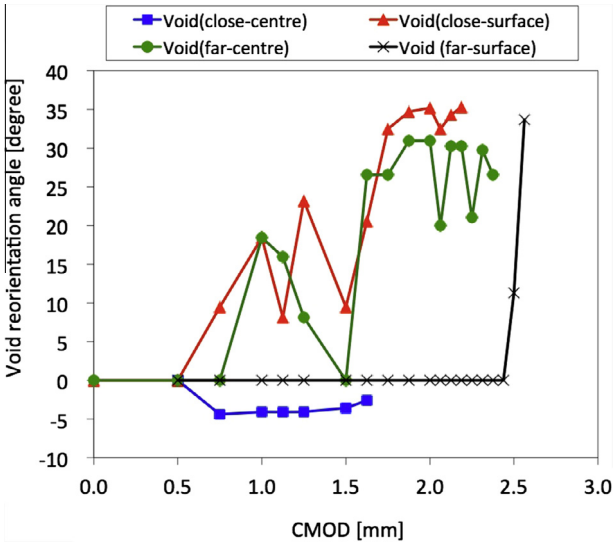

Fig. 14. Evolution of void reorientation angle in the TS plane as a function of CMOD.

an angle of ~45° can be seen in the laminography experiment. However, the result of void reorientation angle in Fig. 14 shows that the maximum reorientation angle is ~30–40°. The relation of void reorientation angle with crack surface is shown in Fig. 15. This indicates that in the region of the slant fracture the voids do not contribute to the crack with their entire surface. A similar result has been observed in Ref. [6] for TWIP steel. The void reorientation happens at late stages of loading, indicating that up to that point plasticity controls the failure process. Other, less ductile materials, such as magnesium alloys, may show slant fracture without micrometric voids at all [46]. It would be interesting to investigate numerically what the contribution of these sheared voids in a localization band to the overall strength is. The localization, however, seems to take place before the voids evolve. Final nucleation of sub-micrometre voids at a second population of smaller second-phase particles in a strain localization band seems to control position of the slant crack. Though the modelling of void shape change in a strain localization band is still challenging [13], interaction between void shape change in a strain localization band and nucleation at a second population of smaller second-phase particles is also an important phenomenon to be modelled to simulate fracture toughness of a thin sheet metal.

5. Conclusion

The mechanisms of individual void evolution and fracture in ductile thin (1.0 mm) sheet metal (AA2139 T3) were investigated using the experimental result obtained by in situ laminography [22] and the FE simulation in the case

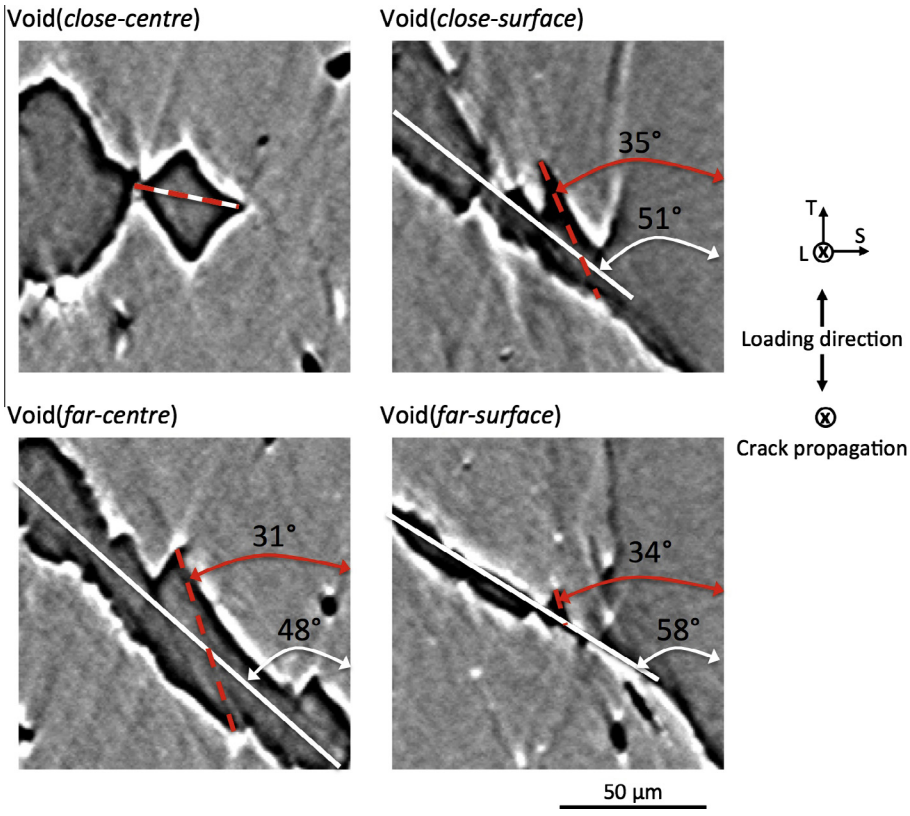

Fig. 15. Comparison of void reorientation angle in red dotted line with crack surface in white line in the experiment. (For interpretation of the references to colour in this figure legend, the reader is referred to the web version of this article.)

of tearing test. The experimental result allowed for quantifying the void behaviour at the positions with different stress and strain histories on the flat and slant cracks. The effect of the mechanical parameters on the behaviour of void evolution such as void volume, Feret dimension and void reorientation angle was investigated using these methods. Four voids were selected: one on the flat crack in the specimen centre and three on the slant crack. One of the voids on the slant crack were in the specimen centre, the other two close to the specimen surface. The main results are summarized as follows:

- The void on the flat crack does not show reorientation whereas the void on the slant crack elongates and tilts towards the slant crack surface.
- Increase of void volume is faster at the centre of the specimen than close to the surface. However, voids close to the surface also show some increase of void volume.
- The void growth/reorientation takes place at very late stages of failure for the voids on the slant crack.
- Regarding Feret dimensions, growth in the T direction is maximal as it is the primary loading direction. Growths in the L and S direction are moderate in the case of voids at the centre of the specimen. However, in the case of voids close to the surface, apparent growth in the nominal S direction is relatively high due to void reorientation.
- The void reorientation angles of the selected voids in the slant area are less than 45°. Reoriented voids do not fully contribute to crack formation and nucleation at a second population of smaller second-phase particles in a strain localization band seems to control position of the slant crack.
- A nucleation of voids on a second population of sub-micrometre particles at a critical strain is needed in the simulations to fit the CMOD crack progression curves. This highlights the fact that the Gurson model, in combination with more classical coalescence criteria f^* [40] trying to account for internal necking, is not able to describe the coalescence process during ductile tearing of Al-alloy sheets.
- Void growth, even using an original form of the GTN model, is overpredicted by the model, indicating early void coalescence in the experiment and the need for better coalescence models.
- The evolution of voids in the experiment shows the same trend/ranking as in the GTN-model simulation for the different voids.

Acknowledgements

The authors would like to acknowledge Ian Sinclair and Mark Mavrogordato from the University of Southampton for participating in/helping with the laminography experiment. Feng Xu is thanked for help with reconstruction of the data. ESRF, beamline ID19, is thanked for beamtime, experiment MA1006.

References

[1] Zerbst U, Heinimann M, Dalle Donne C, Steglich D. Eng Fract Mech 2009;76:5–43.
[2] Anderson TL. Fracture mechanics: fundamentals and applications. 3rd ed. Boca Raton, FL: CRC Press; 2004.
[3] Bron F, Besson J. Eng Fract Mech 2006;73:1531–52.
[4] Bron F, Besson J, Pineau A. Mater Sci Eng A 2004;380:356–64.
[5] Mahgoub E, Deng X, Sutton MA. Eng Fract Mech 2003;70:2527–42.
[6] Lorthios J, Nguyen F, Gourgues-Lorenzon A-F, Morgeneyer TF, Cugy P. Scr Mater 2010;63:1220–3.
[7] Morgeneyer TF, Besson J. Scr Mater 2011;65:1002–5.
[8] Besson J, McCowan CN, Drexler ES. Eng Fract Mech 2013;104:80–95.
[9] Rice JR, Tracey DM. J Mech Phys Solids 1969;17:201–17.
[10] Gurson AL. J Eng Mater Technol 1977;99:2–15.
[11] Gologanu M, Leblond J-B. J Mech Phys Solids 1993;41:1723–54.
[12] Gologanu M, Leblond J-B, Devaux J. J Eng Mater Technol 1994;116:290–7.
[13] Danas K, Ponte Castañeda P. Int J Solids Struct 2012;49:1325–42.
[14] Benzerga AA, Besson J, Pineau A. Acta Mater 2004;52:4623–38.
[15] Maire E, Bouaziz O, Di Michiel M, Verdu C. Acta Mater 2008;56:4954–64.
[16] Maire E, Zhou S, Adrien J, Di Michiel M. Eng Fract Mech 2011;78:2679–90.
[17] Landron C, Maire E, Bouaziz O, Adrien J, Lecarme L, Bareggi A. Acta Mater 2011;59:7564–73.
[18] Toda H, Maire E, Yamauchi S, Tsuruta H, Hiramatsu T, Kobayashi M. Acta Mater 2011;59:1995–2008.
[19] Helfen L, Myagotin A, Mikulík P, Pernot P, Voropaev A, Elyyan M, et al. Rev Sci Instrum 2011;82.
[20] Helfen L, Morgeneyer TF, Xu F, Mavrogordato MN, Sinclair I, Schillinger B, et al. Int J Mater Res 2012;2:170–3.
[21] Xu F, Helfen L, Moffat AJ, Johnson G, Sinclair I, Baumbach T. J Synchrotron Radiat 2010;17:222–6.
[22] Morgeneyer TF, Helfen L, Sinclair I, Proudhon H, Xu F, Baumbach T. Scr Mater 2011;65:1010–3.
[23] Morgeneyer TF, Besson J, Proudhon H, Starink MJ, Sinclair I. Acta Mater 2009;57:3902–15.
[24] Morgeneyer TF, Starink MJ, Sinclair I. Acta Mater 2008;56:1671–9.
[25] Toda H, Oogo H, Uesugi K, Kobayashi M. Mater Trans 2009;50:2285–90.
[26] Taylor KL, Sherry AH. Acta Mater 2012;60:1300–10.
[27] Talbot DEJ. Int Metall Rev 1975;20:166–84.
[28] Morgeneyer TF, Helfen L, Mubarak H, Hild F. Exp Mech 2013;53:543–56.
[29] Helfen L, Baumbach T, Mikulík P, Kiel D, Pernot P, Cloetens P, et al. Appl Phys Lett 2005;86.
[30] Xu F, Helfen L, Baumbach T, Suhonen H. Opt Express 2012;20:794–806.
[31] Weitkamp T, Tafforeau P, Boller E, Cloetens P, Valade J-P, Bernard P, Peyrin F, Ludwig W, Helfen L, Baruchel J. In: Proceedings of 20th international congress X-ray optics and microanalysis, vol. 1221. 2010. p. 33–38.
[32] Rack A, Weitkamp T, Riotte M, Grigoriev D, Rack T, Helfen L, et al. J Synchrotron Radiat 2010;17:496–510.
[33] Sijbers J, Postnovz A. Phys Med Biol 2004;49:247–53.
[34] Helfen L, Baumbach T, Cloetens P, Baruchel J. Appl Phys Lett 2009;94.
[35] Cloetens P, Pateyron-Salomé M, Buffière JY, Peix G, Baruchel J, Peyrin F, et al. J Appl Phys 1997;81.
[36] Beucher S, Lantuéjoul C. Proc Int Workshop Image Process 1979:17–21.

[37] Shen Y, Morgeneyer TF, Garniera J, Allaisa L, Helfen L, Crépin J. Acta Mater 2013;61:2571–82.
[38] Ghahremaninezhad A, Ravi-Chandar K. Int J Solids Struct 2011;48:3299–311.
[39] Besson J, Foerch R. Comput Methods Appl Mech Eng 1997;142:165–87.
[40] Tvergaard V, Needleman A. Acta Metall 1984;32:157–69.
[41] Morgeneyer TF, Taillandier-Thomas T, Helfen L, Sinclair I, Roux S, Baumbach T, et al. Acta Mater 2014;69:78–91.
[42] Steglich D, Wafai H, Besson J. Eng Fract Mech 2010;77:3501–18.
[43] Benzerga AA, Besson J, Batisse R, Pineau A. Mater Sci Eng 2002;10:73–102.
[44] Fleck NA, Hutchinson JW, Tvergaard V. J Mech Phys Solids 1989;37:515–40.
[45] Zhang KS, Bai JB, Francois D. Int J Solids Struct 2001;38:5847–56.
[46] Steglich D, Morgeneyer TF. Int J Fract 2013;183:105–12.